

## A NEW COMPREHENSIVE ANALYSIS TOOL FOR THE PRELIMINARY DESIGN AND DESIGN EVALUATION OF HELICOPTERS – THE CORAL PROJECT

Fred Nitzsche, Christian Spieß, Riekert Leibbrandt  
Kopter Germany GmbH

Altlaufstrasse 34, Höchenkirchen-Siegertsbrunn, 85635, Germany

Massimo Gennaretti, Giovanni Bernardini, Jacopo Serafini, Federico Porcacchia  
Roma Tre University

Via della Vasca Navale 79, 00146, Rome, Italy

Vasilis Riziotis, Giorgios Papadakis, Nikos Spyropoulos  
iWind / National Technical University of Athens  
Iroon Polytechniou str. 9, 15780, Zografou, Greece

Ali Siami, Doma Hilewit, Mohammad Rafiee  
Rotorcraft Research Group, Carleton University  
1125 Colonel By Drive, K1S 5B6, Ottawa, Canada

### Abstract

Designing modern VTOL vehicles is a complex task that demands the interaction of disciplines such as flight mechanics, structural analysis, aerodynamics, dynamics and control, aeroelasticity, power systems and avionics. In addition, aeroacoustics has also become crucial as the certification authorities enforce to the manufacturers more restrictive environmental noise impact concerns. The project CORAL (Comprehensive Rotorcraft Analyses Lab) is concerned with the integration of all these disciplines, except for power systems and avionics, into a single easy-to-adapt and user-friendly simulation tool that allows for comprehensive analyses of not only conventional helicopter configurations but also non-conventional VTOL vehicles.

### 1. INTRODUCTION

The CORAL project involves partners in Italy (University Roma Tre – RM3), Greece (National Technical University of Athens and the consulting company iWind) and Canada (Carleton University's Rotorcraft Research Group – CU) under the coordination of Kopter Germany, a member of the Leonardo Group.

---

#### Copyright Statement

*The authors confirm that they, and/or their company or organization, hold copyright on all of the original material included in this paper. The authors also confirm that they have obtained permission, from the copyright holder of any third-party material included in this paper, to publish it as part of their paper. The authors confirm that they give permission or have obtained permission from the copyright holder of this paper, for the publication and distribution of this paper and recorded presentations as part of the ERF proceedings or as individual offprints from the proceedings and for inclusion in a freely accessible web-based repository.*

The objective of this paper is to report the progresses made in the first phase of the project. From Figure 1, the organization of the simulation tool is understood: the input data (represented by black boxes) are the vehicle geometric, structural, inertia data, the rotors control models and pre-established steady flight conditions in the first phase of the project. The latter restriction will be relaxed in later phases of the project. The simulation tool encompasses the coordination of specific moduli and functions (indicated by the orange boxes) to produce the required outputs (denoted in the green boxes). As seen in Figure 1, the VTOL vehicle is fundamentally modeled as an aeroelastic system. The aeroelastic loop assembles the aerodynamic and structural dynamics moduli to perform non-linear aeroelastic analyses, creating the entire vehicle's structural loads and deflections at given flight conditions. The Trim

Function depicted in the same figure provides the attitude angles; it considers rotors thrust forces, rolling and pitching moments corresponding to the trim conditions. One of the most important features of CORAL is that the aeromechanic model can be linearized about its trim state and a Reduced-order Model (ROM) built using a model identification technique developed by RM3 [1.]. The ROM is then used by the Flight Dynamics Module to access at lower computational costs the vehicle handling qualities due to pilot input. The aeromechanic stability and linear response to arbitrary external

inputs such as gusts use the ROM as well rather than the original nonlinear aeromechanic model.

Note also that in CORAL, a ROM approach is applied also for the analysis of the rotor aeroelastic stability. In this case, a linearized, multiblade variables ROM description of the unsteady rotor aerodynamics, as derived from the high-fidelity aerodynamic solver in [1.] and [2.], allows for the evaluation of the rotor aeroelastic eigenvalues and eigenvectors and, hence, the identification of its limit of stability.

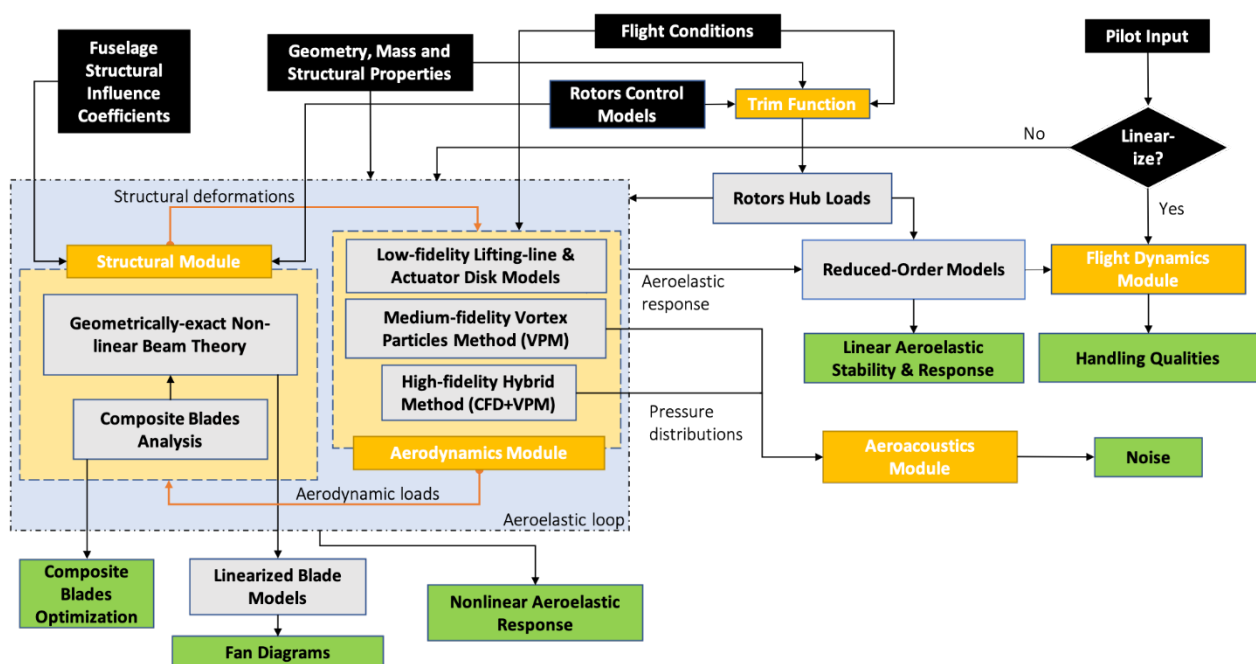


Figure 1: CORAL comprehensive simulation tool structure.

## 2. AEROMECHANIC MODEL

### 2.1. The Aerodynamic Module

The Aerodynamic Module includes different options that allow for a compromise between computational accuracy and efficiency: 1) a standard lower-fidelity actuator disk and blade element momentum model able to simulate rotors alone without considering their mutual interaction and the fuselage effects. 2) The next model in order of accuracy and complexity is a medium-fidelity free-vortex wake model based on the incompressible potential flow theory. It

offers a panel modelling of the fuselage and uses the Vortex-Particles Method (VPM) with corrections based on pre-calculated 2D airfoil polar data to account for viscous effects due to drag, flow separation and compressibility effects. Under this option, interactions between different aerodynamic components are considered as well as the possibility to model shrouded rotors. 3) The most accurate and complex model comprises a higher-fidelity

hybrid methodology, which combines the Eulerian CFD and the Lagrangian approaches. It couples an unstructured CFD solver for the domain close to solid boundaries with a compressible particle solver based on the VPM strategy for the far field developed by iWind / NTUA [3.], [4.]. With the hybrid option, besides being able to capture interactions between different aerodynamic components, the possibility to model shrouded rotors and fuselage aerodynamic loads is offered. Furthermore, the hybrid CFD option offers the possibility to perform fully resolved simulations of the helicopter rotors when detailed aerodynamic performance analysis is required but also an Actuator Line (AL) option which is better suited for computationally intense time domain aeroelastic simulations [5.].

### 2.1.1. Medium-fidelity free-wake model

The core theory of CORAL VPM aerodynamic model utilizes the Helmholtz decomposition theorem, through which the influence of solid body components such as rotor blades, fuselage, and stabilizers are captured along with the influence of their wakes.

Consider the unsteady flow of an incompressible and inviscid fluid around a general multi-component configuration. The bodies are allowed to move independently, a necessary feature for any VTOL configuration. Therefore, in CORAL a group of individual bodies, each described by a set of input files that define both the configuration geometrical characteristics and kinematics, is considered. As seen in Figure 2, in the context of the free wake code, aerodynamic bodies (e.g., rotating or fixed wings) can be considered as 1) *lifting lines*, 2) *thin lifting surfaces* or 3) *thick panel bodies*. All aerodynamic bodies are divided into a number of “cross sections” which are defined perpendicular to the body reference line. Furthermore, a number of nodal points are defined over every cross section. The wing element between two consecutive sections forms the “strip”. The strip is the main aerodynamic entity of the body, on which the local aerodynamic loads are calculated.

In the lifting line analysis, each section has only two nodes describing the leading and trailing edge of the airfoil, which, therefore, collapses into a single flat plate element (panel), formed

on each strip as shown in Figure 2. In the lifting surface and thick panel analysis, the building block of the numerical grid is the surface panel element formed by four grid nodes (two pairs belonging to consecutive sections) in clockwise direction. In this case, a number of surface elements (panels), as shown in Figure 2, forms the strip. Inside every panel, a single control point (collocation point) is defined, on which the local pressure (for thick bodies) or the pressure jump (for thin bodies) or yet the circulation (for lifting line bodies) is calculated. Free wake vortex lattice type panels are emitted from the trailing edge nodes of the sections of the lifting bodies to compose the near field (Figure 3).

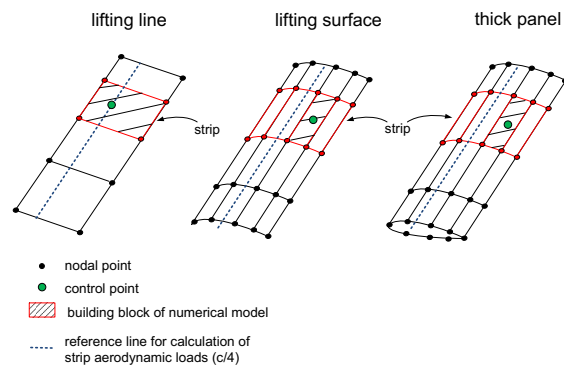


Figure 2: CORAL basic body approaches (lifting line, thin body and thick body).

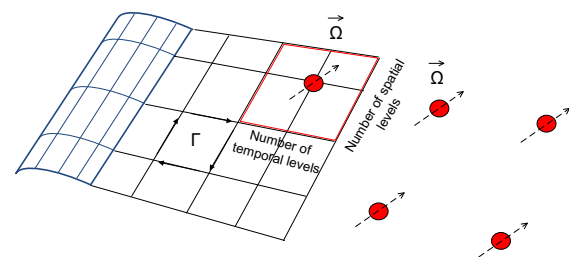


Figure 3: CORAL vortex particles generation.

Once they move away from the body, in a subsequent number of time steps, the wake panels are converted into vortex particles, which compose the far field. This is done by integrating the vorticity of each near-wake vortex lattice element to form a vortex particle [6.]. Like the vortex lattice part of the wake, vortex particles are also free to move with the local flow velocity. The extent of the vortex lattice wake is a user-defined parameter that is

usually set between half and one revolution. When integrating the vorticity of the wake filaments to generate wake particles, the possibility of merging wake elements into the temporal and spatial direction (as seen in Figure 3), which leads to substantial computational time saving, is also given to the user.

As per Helmholtz's theorem of vector calculus, the total instantaneous velocity of a control points situated at  $\vec{x}_0$  at a determined time step is given by:

$$(1) \quad \vec{u}(\vec{x}_0; t) = \vec{u}_{ext}(\vec{x}_0; t) + \vec{u}_{solid}(\vec{x}_0; t) + \vec{u}_{wake}(\vec{x}_0; t)$$

In (1), the first component is associated with the given time-varying external field. The second component accounts for the solid boundaries expressed, according to Green's theorem, by surface singularity distributions. In the lifting line approach, body contribution is considered by open "horseshoe" shape vortex filaments distributed over the strips. In the lifting surface and thick panel options, the body contribution is considered by dipole and dipole plus source distributions, respectively, over the elements. The third component includes the body wakes, which are composed by vortex filaments or vortex particles. For this, Biot-Savart's law is used:

$$(2) \quad \begin{aligned} \vec{u}_{wake}(\vec{x}_0; t) &= \\ &= \int_{D_{\omega(t)}} \frac{\vec{\omega}(\vec{x}; t) \times (\vec{x}_0 - \vec{x})}{4\pi|\vec{x}_0 - \vec{x}|^3} dD \end{aligned}$$

In (2), the integration is carried over the entire computational domain,  $D_{\omega(t)}$  where the individual particles vorticity vectors,  $\vec{\omega}(\vec{x}; t)$  still maintain a significant contribution to the local velocity,  $\vec{u}_{wake}(\vec{x}_0; t)$ . The local velocities are computed at both the panels control points and every particle in the field, thereby generating the wake deformation in time.

In the *lifting line* option, every strip bound circulation,  $\vec{\Gamma}(\vec{x}_0; t)$  is obtained from the solution of the discretized system of equations:

$$(3) \quad \vec{L}(\vec{x}_0; t) = \rho \vec{u}(\vec{x}_0; t) \times \vec{\Gamma}(\vec{x}_0; t)$$

The nonlinear equation, (3) is satisfied at every control point of the lifting line grid, i.e., at the strip single control point located at the quarter-

chord line in the midspan position of the strip. This solution uses as input the airfoil 2D polar characteristics at spanwise sections; corrections based on ONERA's model [7.] are applied to account for dynamic stall effects.

In the case of the *thin lifting surface* and *thick panel body* options, the non-penetration kinematic boundary condition is satisfied at the control points. In this case, at the center point of every surface panel element. In addition, the Kutta condition is satisfied along the trailing edge (TE) line of all lifting bodies. In the latter two modeling options, there is no need for the definition of the airfoil polar characteristics, except when applying viscous corrections. As in the lifting line case, this is done on a-posteriori basis, using the ONERA dynamic stall model. For *non-lifting bluff bodies*, the procedure is the same as for lifting *thick bodies* except that no Kutta condition is satisfied and, thus, no wake emission takes place.

A simulation example of a complete helicopter configuration using the medium-fidelity model is depicted in Figure 4.

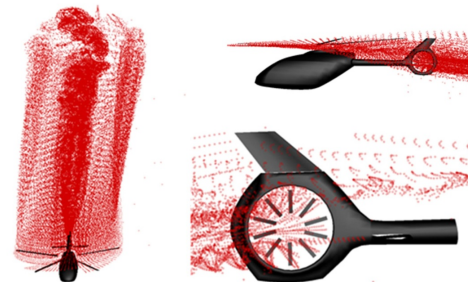


Figure 4: (Left) Complete helicopter simulation with its wake patter; (right) interaction details of the main rotor wake with the empennage and tail rotor.

### 2.1.2. High-fidelity hybrid CFD model

CORAL's hybrid High-fidelity CFD methodology combines the conventional grid based CFD with the particle (Lagrangian) methods. A CFD component solves the Unsteady Reynolds-Averaged Navier Stokes (URANS) equations. This is a compressible, cell centered CFD solver, which employs both structured and unstructured grids. The convective fluxes are discretized using the approximate Riemann solver of Roe [8.] with the Venkatakrishnan limiter [9.], while the viscous fluxes are discretized using a central second-order scheme. Turbulence closure includes several

options; the single equation turbulence model of Spalart (SA) [10.], as well as the double equation turbulence model of Menter (k- $\omega$  SST) [11.]. The solver can handle both steady and unsteady flows; the latter being an important requirement for aerodynamic tools employed in aeroelastic analyses. Time integration is carried out in an implicit manner permitting large CFL numbers. The unsteady calculations use a second-order time accurate scheme combined with the dual time-stepping technique [12.] to facilitate convergence when complex unsteady flows with moving or deforming geometries are considered. Additionally, flows in the incompressible region are realized using low-Mach preconditioning [13.].

In the application of the hybrid model, the CFD grid is confined around the solid boundaries and may be composed of more than one disjoint sub-domains (one dedicated per separate solid component, e.g., a blade). In this way, all solid boundaries are associated to the CFD part of the solver, which can efficiently impose the appropriate boundary conditions.

The CFD sub-domains also need outer boundary conditions, which are no longer in the far field. They are interfaces on which the complete flow information is needed. This is provided by a background flow field defined in particle form. Particles carry mass, dilatation, vorticity and pressure, and cover the *entire flow domain*. Therefore, they overlap with the gridded CFD domains (as seen in Figure 5). Such overlap allows for communication of the flow information between the gridded CFD and the VPM solutions. To ensure the continuity and compatibility of the two solutions, a strong coupling between them is imposed through an iterative process.

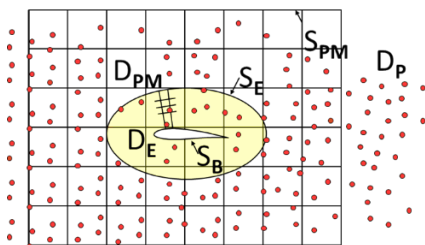


Figure 5: The domain decomposition.

However, a decisive cost reduction of the particle (Lagrangian) solution is accomplished by using the Particle Mesh (PM) technique [14.]

combined with multi-block Fast Poisson solvers [15.]. In PM, the governing equations are solved on a Cartesian grid and, subsequently, the solution is interpolated at the particle positions.

More details on the hybrid method, in particular details on the coupling procedure between the two methods (Eulerian – Lagrangian) can be found in [4.]. In Figure 6, the hybrid scheme is shown for a four bladed rotor representation in the forward flight condition.

## 2.2. The Structural Module

Multibody dynamics (MBD) is adopted in the modelling of all structural components of the rotor assembly. This not only includes the blades, but also the flexible elements of the control chain of the helicopter’s main and tail rotors (blade hub, pitch link, horn etc.). In the MDB analysis, all flexible components are represented as 1D flexible beam structures. Flexible elements of the control chain are model as linear Timoshenko beam elements. Rotor blades are modeled as geometrically exact nonlinear beams (following Hodges’ intrinsic formulation [16.]). Numerical discretization is user defined and based either on FEM analysis or Galerkin’s approach.

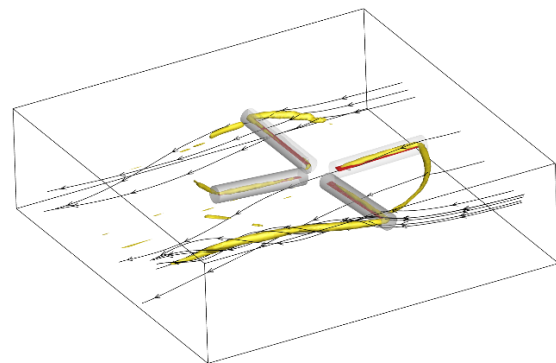


Figure 6: Iso-surface of Q criterion for a 4-bladed rotor in forward flight. The PM grid covers the whole domain while the truncated CFD grids (in grey) are defined only in the near blade region (in red).

MBD can concurrently accommodate rigid body motions and structural flexibilities, together with the nonlinear inertial and structural effects, and the geometric couplings that large deflections of the highly flexible components introduce (e.g., blades). Rigid-body motions are imposed by either the control system (blades pitch, vehicle

response to pilot's input, drive train rotational speed) or external excitations (effect of inflow / environmental conditions to vehicle kinematics).

Regarding the MBD scheme kinematics, Figure 7 depicts the local coordinate systems,  $[O, x, y, z]$  that are assigned to all individual body components.

The local elastic displacements are defined with respect to these frames. Hence, the local frame of each body is subjected to both (a) rigid body and (b) elastic motions. For the  $k^{\text{th}}$  body, let

$\mathbf{q}^k = \{\mathbf{q}_t^k, \mathbf{q}_r^k\}^T$  denote a set of time-

invariant and / or time-variant rigid-body displacements and rotations that define both the origin and orientation of the  $k^{\text{th}}$  body local system in the undeflected state. The  $\mathbf{q}^k$  vector

contains: i) all translations and rotations that in the unmoved / undeflected state define body's local coordinate system with respect to the inertial frame, ii) time-variant body self-motions (e.g., pitch angle of the blades), iii) global rigid-body kinematic degrees of freedom collectively undergone by the bodies, including the  $k^{\text{th}}$  body (e.g., rotor rotational speed, global vehicle

motions). In addition,  $\mathbf{q}_0^k = \{\mathbf{q}_{0t}^k, \mathbf{q}_{0r}^k\}^T$  is a 6-component vector including 3 translations and 3 rotations induced by the motions of other bodies connected to the  $k^{\text{th}}$  body, such as those resulting from their elastic motions (see Figure 8).

As a result of the afore defined motions, the origin of the local body system is displaced by  $\mathbf{R}_P^k$  and  $\mathbf{R}_0^k$ , respectively, and its axes are, correspondingly, rotated by the matrices  $\mathbf{T}_P^k$  and  $\mathbf{T}_0^k$ , as indicated in Figure 8.

Figure 7 shows the *global* position vector  $\mathbf{r}_G^k$  of any arbitrary point over the deflected  $k^{\text{th}}$  body with respect to the global inertia frame,  $[O_G, x_G, y_G, z_G]$ . This global position vector is composed by: a vector defining a point in the undeflected state,  $\mathbf{r}_l^k = (x_l^k, y_l^k, z_l^k)^T$ ; a vector associated with the corresponding elastic

deflections,  $\mathbf{u}^k$  likewise defined in body local coordinates and, implicitly, by the  $k^{\text{th}}$  body motion characterized by the vectors  $\mathbf{q}^k$  and  $\mathbf{q}_0^k$ , as follows:

$$\mathbf{r}_G^k = \underbrace{(\mathbf{R}_P^k(\mathbf{q}^k; t) + \mathbf{T}_P^k(\mathbf{q}_r^k; t) \cdot \mathbf{R}_0^k(\mathbf{q}_0^k; t))}_{\mathbf{R}^k} + \underbrace{\mathbf{T}_P^k(\mathbf{q}_r^k; t) \cdot \mathbf{T}_0^k(\mathbf{q}_{0r}^k; t)}_{\mathbf{T}^k} \cdot (\mathbf{r}_l^k + \mathbf{u}^k(t)) \quad (4)$$

A variety of kinematic constraint equations (e.g., rigid or elastic displacements / rotations, free relative rotations) are defined for the degrees of freedoms: (a)  $\mathbf{q}_0$  of the connected bodies and, (b)  $\mathbf{q}$  global time-variant associated with the additional kinematic and / or dynamic equations that need to be defined. Besides kinematic constraint equations, dynamic compatibility conditions need to be applied to the connected bodies. Especially, when two or more bodies are connected to each other, one body (at a particular node) defines the kinematics, and the others provide reaction loads. These reaction loads (3 forces and 3 moments per body) are thus applied as external point forces / moments to the node that defines the kinematics.

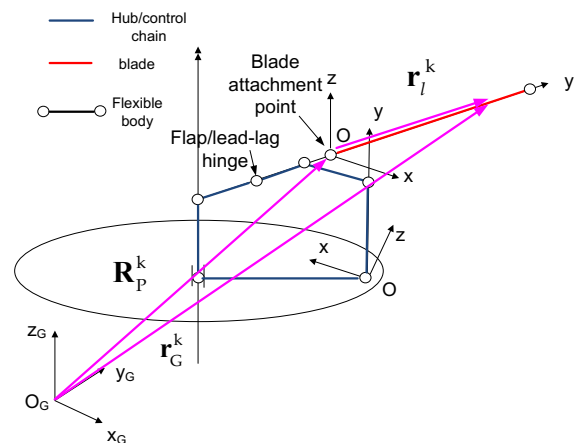


Figure 7: Simple model of a main rotor control chain. Examples of local co-ordinate systems of connected bodies.

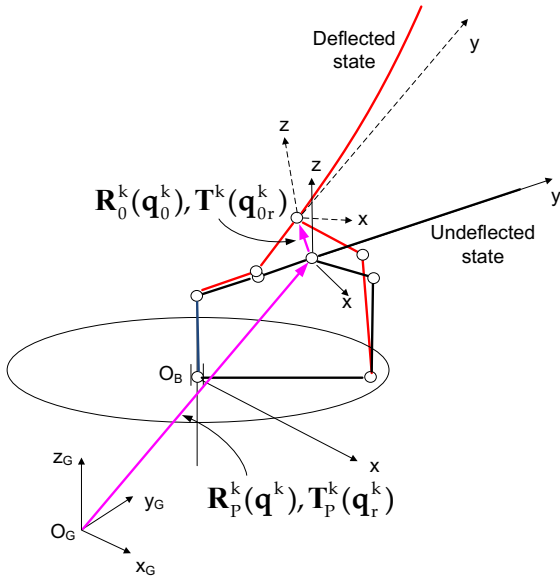


Figure 8: Simple model of a main rotor control chain. Definition of  $\mathbf{q}^k$  and  $\mathbf{q}_0^k$  vectors.

In particular, the analysis of the flexible blades is based on the geometrically exact beam theory that involves the solution of the nonlinear, intrinsic equations describing the dynamic response of rotating composite beams undergoing large deformations. The major accomplishment of the geometrically exact beam theory is that the linear material laws valid for small local strains can, however, generate large global deformations.

The nonlinear, intrinsic, mixed equations for the dynamics of a general (non-uniform, twisted, curved, anisotropic) beam undergoing small strains and large deformations are [16.]:

$$(5a) \quad \mathbf{F}' + (\tilde{\mathbf{k}} + \tilde{\boldsymbol{\kappa}})\mathbf{F} + \mathbf{f} = \dot{\mathbf{P}} + \tilde{\boldsymbol{\Omega}}\mathbf{P}$$

$$(5b) \quad \mathbf{M}' + (\tilde{\mathbf{k}} + \tilde{\boldsymbol{\kappa}})\mathbf{M} + (\tilde{\boldsymbol{\epsilon}}_1 + \tilde{\boldsymbol{\gamma}})\mathbf{F} + \mathbf{m} = \dot{\mathbf{H}} + \tilde{\boldsymbol{\Omega}}\mathbf{H} + \tilde{\mathbf{V}}\mathbf{P}$$

$$(5c) \quad \mathbf{V}' + (\tilde{\mathbf{k}} + \tilde{\boldsymbol{\kappa}})\mathbf{V} + (\tilde{\boldsymbol{\epsilon}}_1 + \tilde{\boldsymbol{\gamma}})\boldsymbol{\Omega} = \dot{\boldsymbol{\gamma}}$$

$$(5d) \quad \boldsymbol{\Omega}' + (\tilde{\mathbf{k}} + \tilde{\boldsymbol{\kappa}})\boldsymbol{\Omega} = \dot{\boldsymbol{\kappa}}$$

In (5a-d), the prime denotes partial derivative with respect to the non-deformed beam reference line, defined by the curvilinear coordinate. Note from Figure 9, the undeformed state axial coordinate along the blade is here denoted by  $x$  following Hodges' [16.], which is in the direction of  $y$  according to Figure 8. The internal forces and moments vectors are

respectively denoted by  $\mathbf{F}(x, t)$  and  $\mathbf{M}(x, t)$ ;  $\mathbf{P}(x, t)$  and  $\mathbf{H}(x, t)$  are the linear and angular momentum vectors;  $\boldsymbol{\gamma}(x, t)$  and  $\boldsymbol{\kappa}(x, t)$  are the generalized strain and curvature vectors;  $\mathbf{V}(x, t)$  and  $\boldsymbol{\Omega}(x, t)$  are the linear and angular velocity vectors. The external force and moments due to aerodynamic and disturbance (such as control) effects are generically denoted by  $\mathbf{f}(x, t)$  and  $\mathbf{m}(x, t)$ , where the superscripts "aero" and "dist" are added to these variables to discriminate them if necessary. The beam undeformed spanwise and chordwise curvatures,  $k_2$  and  $k_3$  and the twist,  $k_1$  are collected into the generalized curvature vector,  $\mathbf{k} = [k_1 \ k_2 \ k_3]^T$  and  $\mathbf{e}_1 = [1 \ 0 \ 0]^T$ . Finally, the tilde over certain vectors denotes an operation with its components, transforming it into a skew-symmetric matrix, such as:

$$(6) \quad \tilde{\mathbf{K}} = \tilde{\mathbf{k}} + \tilde{\boldsymbol{\kappa}} = \begin{bmatrix} 0 & -K_3 & K_2 \\ K_3 & 0 & -K_1 \\ -K_2 & K_1 & 0 \end{bmatrix}$$

These intrinsic beam equations provide four vector equations for the eight unknown vector quantities,  $(\mathbf{F}, \mathbf{M}, \mathbf{P}, \mathbf{H}, \boldsymbol{\gamma}, \boldsymbol{\kappa}, \mathbf{V}, \boldsymbol{\Omega})$ . Therefore, four more vector equations are needed to provide a closed mathematical solution. Two equations relate the generalized forces,  $(\mathbf{F}, \mathbf{M})$  and the generalized strains  $(\boldsymbol{\gamma}, \boldsymbol{\kappa})$  via the cross-section flexibility matrix:

$$(7) \quad \begin{Bmatrix} \boldsymbol{\gamma} \\ \boldsymbol{\kappa} \end{Bmatrix} = \begin{bmatrix} \mathbf{R} & \mathbf{S} \\ \mathbf{S}^T & \mathbf{T} \end{bmatrix} \begin{Bmatrix} \mathbf{F} \\ \mathbf{M} \end{Bmatrix}$$

where the coefficients of the  $3 \times 3$  matrices  $\mathbf{R}$ ,  $\mathbf{S}$  and  $\mathbf{T}$  can be obtained using computational methods, such as the one presented in [17.].

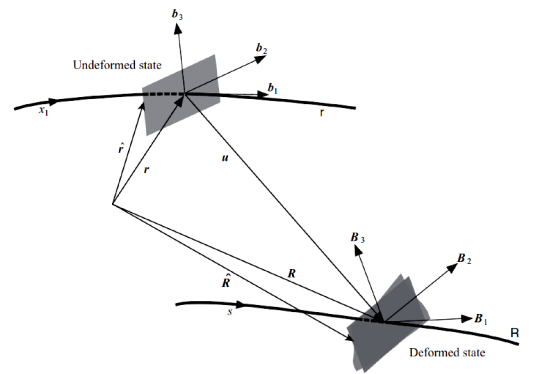


Figure 9: Schematic of a beam in two different states under finite deformation and cross-sectional warping [16.].

The cross-section inertia matrix introduces a relationship between the generalized momenta ( $\mathbf{P}, \mathbf{H}$ ) and the generalized velocities ( $\mathbf{V}, \mathbf{\Omega}$ ):

$$(8) \quad \begin{cases} P_1 \\ P_2 \\ P_3 \\ H_1 \\ H_2 \\ H_3 \end{cases} = \begin{bmatrix} \mu & 0 & 0 & 0 & \mu\bar{x}_3 & -\mu\bar{x}_2 \\ 0 & \mu & 0 & -\mu\bar{x}_3 & 0 & 0 \\ 0 & 0 & \mu & \mu\bar{x}_2 & 0 & 0 \\ 0 & -\mu\bar{x}_3 & \mu\bar{x}_2 & i_2 + i_3 & 0 & 0 \\ \mu\bar{x}_3 & 0 & 0 & 0 & i_2 & i_{23} \\ -\mu\bar{x}_2 & 0 & 0 & 0 & i_{23} & i_3 \end{bmatrix} \begin{cases} V_1 \\ V_2 \\ V_3 \\ \Omega_1 \\ \Omega_2 \\ \Omega_3 \end{cases}$$

where  $\mu$  is the mass per unit length,  $\bar{x}_2$  and  $\bar{x}_3$  are the center of mass offsets from the beam reference axis;  $i_2$ ,  $i_3$  and  $i_{23}$  are, respectively, the cross-sectional momenta and product of inertia per unit length about the reference axis.

## 2.3. The Trim Function

### 2.3.1. Scope

The scope of the trim module is to determine the rotorcraft attitude angles and the hub loads corresponding to a pre-defined steady-state flight condition (see Figure 1).

As typical for any trim solver, this module is also capable to predict the required pilot inputs. However, these inputs are not used in the solution process because they are strongly dependent on the rotor aerodynamic model, which, as usual in trim solution schemes, is of a low-fidelity type. Instead, it is the higher fidelity aeroelastic module, which complies with the vehicle attitude and hub loads predicted by the trim module, that updates the pilot inputs.

### 2.3.2. Solving scheme

Under the assumption of stationary flight conditions and fixed pilot commands, the set of ordinary differential equations governing the flight dynamics [18.] are transformed into a set of nonlinear algebraic equations that are solved iteratively for the roots using the Newton Raphson technique. The procedure workflow is presented in Figure 10.

Specifically, the process starts with the trim variables initial guess. Then, the subsequent iterations are targeted to balance the steady-state forces and moments from all helicopter sub-components.

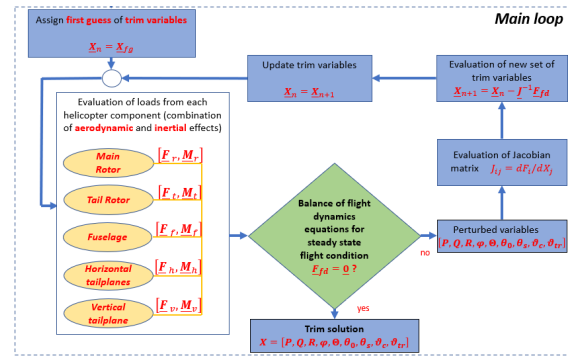


Figure 10: Trim module solving scheme

Loads from main and tail rotor, fuselage, as well as the horizontal and vertical empennages, are determined by assuming that they are aerodynamically isolated bodies; however, correction coefficients are used to take into account interactional aerodynamic effects [19.].

The aerodynamic loads acting on main and tail rotor are evaluated through a quasi-steady strip-theory model combined with a look-up table technique for the identification of the sectional aerodynamic coefficients. Three-dimensional flow corrections are applied by introducing a wake inflow model based on the momentum / modified momentum theory and the blade tip losses through the Prandtl function [20.].

The main rotor hub loads are determined from the periodic solution of the “internal” dynamics of rigid blades, free to rotate about the flap, lag and pitch hinges located at arbitrary distances from the hub, based on the harmonic-balance method [21.], where it was validated for the nonlinear aeroelastic analyses of moderate-displacement elastic rotor blades. The aerodynamic loads from the vertical and horizontal empennages are included through a look-up table using predetermined aerodynamic data. Here, one of the following two options are available; use 1) the sectional aerodynamics combined with lift deficiency factor taking into account the finite span of the wings or, 2) force and moment coefficients directly obtained from aerodynamics of three-dimensional bodies. Similarly, the fuselage loads are included using the look-up table technique, in this case based on aerodynamic data of three-dimensional bluff bodies. Also included in the solution are the interactional aerodynamic effects, namely: 1)

the influence of the main rotor wake inflow on the effective angle of attack and dynamic pressure of the horizontal tail, 2) the fuselage shadow and main rotor wake inflow on the effective dynamic pressure of the vertical fin and 3), the fuselage influence on the main rotor inflow throughout an induced upwash [19].

### 3. THE AEROACOUSTIC MODULE

The aeroacoustic solver is based on the compact-source version of the Farassat 1A boundary integral formulation seen in [22.], [23.], [24.] for the solution of the Ffowcs Williams and Hawkings equation [25.]. Under the assumptions of negligible blade chord-length with respect to the source-observer distance, and limited values of chordwise pressure gradients, this *compact formulation* has been shown to be an excellent tool for prediction of the rotorcraft aerodynamically generated near-field noise [22.], [24.], [26.]. It provides a good balance between satisfactory accuracy of predictions and computational performance, while also limiting the amount of data exchange between the aerodynamic and the aeroacoustic solvers [22.].

For rotors in subsonic regime, the formulation yields the aeroacoustic pressure field as superposition of two terms: 1) the *thickness noise*,  $p'_T$  dependent on the blade geometry and kinematics, and 2) the *loading noise*,  $p'_L$  associated to the blade airload. Assuming a slender rotor blade, the *thickness noise term* can be expressed as the combination of line integral contributions along the spanwise quarter-chord line,  $D_s$ , [23.]:

$$(9) \quad \begin{aligned} & \frac{4\pi}{\rho_0} p'_T(\mathbf{x}, t) \\ &= \int_{D_s} \left[ \frac{A \dot{W}}{r^2 |1 - M_r|^4} \right]_{\tau} ds(\mathbf{y}) \\ &+ 3 \int_{D_s} \left[ \frac{A W^2}{r^3 |1 - M_r|^5} \right]_{\tau} ds(\mathbf{y}) \\ &- c_0 \int_{D_s} \left[ \frac{A M_r W}{r^3 |1 - M_r|^4} \right]_{\tau} ds(\mathbf{y}) \end{aligned}$$

where  $W = r \dot{\mathbf{M}} \cdot \hat{\mathbf{r}} + c_0(M_r - M^2)$ .

In (9),  $A$  is the blade cross sectional area,  $s$  is the spanwise (curvilinear) coordinate,  $c_0$  and  $\rho_0$  are the speed of sound and the density of the undisturbed medium,  $\mathbf{M} = \mathbf{v}_B/c_0$  is the blade

Mach vector, with  $\mathbf{v}_B$  denoting the blade velocity vector,  $M = \|\mathbf{M}\|$  and  $M_r = \mathbf{M} \cdot \hat{\mathbf{r}}$ , where  $\hat{\mathbf{r}} = \mathbf{r}/r$  is the unit vector with magnitude  $r = \|\mathbf{y} - \mathbf{x}\|$  between the observer point  $\mathbf{x}$  and the blade source point,  $\mathbf{y}$ . The dot accent denotes the time derivative observed from a frame of reference fixed in the undisturbed medium. The notation  $( )_{\tau}$  indicates quantities that must be evaluated at the emission time,  $\tau$ , i.e., the time at which a signal arriving in  $\mathbf{x}$  at time  $t$  was emitted at  $\mathbf{y}$  [27.].

Still using the compact-source assumption ([22.], [24.]) the following for the *loading noise* term is obtained:

$$(10) \quad \begin{aligned} & 4\pi p'_L(\mathbf{x}, t) \\ &= \frac{1}{c_0} \int_{D_s} \left[ \frac{\dot{\mathbf{L}} \cdot \hat{\mathbf{r}}}{r |1 - M_r|^2} \right]_{\tau} ds(\mathbf{y}) \\ &+ \int_{D_s} \left[ \frac{\mathbf{L} \cdot (\hat{\mathbf{r}} - \mathbf{M})}{r^2 |1 - M_r|^2} \right]_{\tau} ds(\mathbf{y}) \\ &+ \int_{D_s} \left[ \frac{\mathbf{L} \cdot \hat{\mathbf{r}}}{r^2 |1 - M_r|^3} \left( \frac{r \dot{\mathbf{M}} \cdot \hat{\mathbf{r}}}{c_0} + M_r - M^2 \right) \right]_{\tau} ds(\mathbf{y}) \end{aligned}$$

where  $\mathbf{L}$  is the blade sectional force vector, which is only significantly produced by the lift in this case:

$$(11) \quad \mathbf{L} = - \int_{D_c} \Delta p \hat{\mathbf{n}} dl$$

Here,  $D_c$  is the chordwise domain of integration (airfoil mean-line),  $l$  is the corresponding (curvilinear) coordinate and  $\hat{\mathbf{n}}$  and  $\Delta p$  are, respectively, the upward unit normal to the airfoil mean-line and its pressure jump distribution across the upper and lower surfaces. Note that this formulation predicts the same loading noise contribution for any chordwise pressure field with the same spanwise distribution of sectional forces,  $\mathbf{L}$ .

The compact formulation is a particular case of the more general formulation presented in [24.], particularly suitable for application in the rotorcraft conceptual / preliminary design phases. It is also suitable for the analyses of helicopters in maneuvering flight [28.], [29.], [30.] and [31.].

## 4. RESULTS AND VALIDATIONS

### 4.1 Aeromechanic validations

A first attempt to compare predictions of CORAL aeroelastic module, against flight test load data of the main rotor (MR) of the Kopter SH09 helicopter prototype is presented in this section. Both the flexible blades and the flexible elements of the rotor hub are considered in the aeroelastic analysis of the MR assembly. An example of the aeroelastic setup is depicted in Figure 11. As shown in the plot, the lifting bodies modeled using lifting line method along with their numerical grid are represented by grey surfaces (aerodynamic strips – see Section 2.2.1, Figure 2), while red segments represent flexible beam elements. The symbols over the red lines correspond to the nodes of the FEM grids. The flexible hub of the SH09 consists of a non-aerodynamic flexible holder connected to the inboard part of the blade – the blade/holder attachment point. The holder is attached to a flexible housing at its root. Furthermore, the holders of consecutive blades are inter-connected by lead-lag dampers forming the polygon line seen in Figure 11. The dampers are simulated by two connected beams, which are allowed to slide the one with respect to the other in the direction along-wise the beam axes.

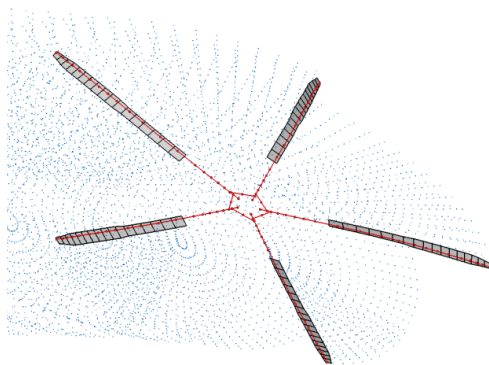


Figure 11: MR aeroelastic setup. Lifting surfaces are depicted in grey color. Red segments represent flexible bodies-elements.

Representative predictions of the flapwise bending moment at  $r/R=0.36$  are shown in Figure 12 in comparison to flight test data for a forward flight case with flight speed of 110 KTAS. The results presented in the plot

correspond to azimuthal variation of the flapwise moment normalized by its maximum positive value. Predictions of Figure 12 are obtained after trimming the control angles of the simulation in order to match the measured hub loads. Moreover, the actual helicopter attitudes measured during the flight test are considered in the aeroelastic simulation.

As seen in Figure 12, predictions capture relatively well the mean value of the measured signal. A small under-prediction in the amplitude and a slight shift in the phase of the 1/rev variation are noted with respect to the measured signal. Furthermore, simulations seem to considerably over-predict the amplitude of 3/rev harmonic.

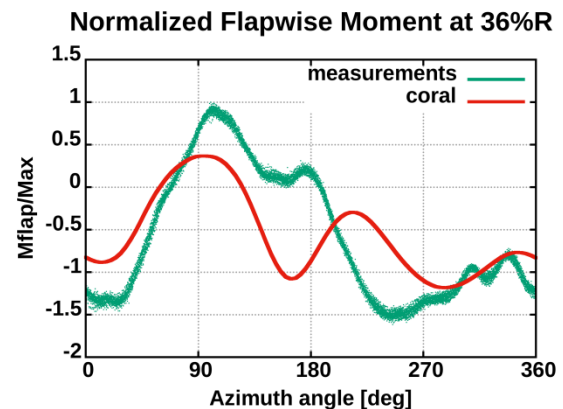


Figure 12: Flapwise bending moment at  $r/R=0.36$ . Comparison against flight test data.

### 4.2 Aeroacoustic results

The following aeroacoustic results are obtained by applying the compact-sources version of the Farassat 1A formulation presented in Section 3. The predicted radiated noise is presented in terms of A-weighted dB scales (dBA) of the Overall Sound Pressure Level (OASPL). Particular attention is paid to the capability of the CORAL tool to account for the effects of main-tail rotors interactional aerodynamics on the helicopter noise signature. To assess the impact of the higher-frequency contributions of the tail rotor on the human perceived noise, two versions of the OASPL are used: one evaluated in the frequency range 0-40 main rotor BPFs, and one evaluated in the extended range 0-296 BPFs. Aeroacoustic footprints are computed over a hemisphere of radius 150 m, rigidly connected to the helicopter, that is located at its

center. Results are produced for both a fly-over and a descent flight.

#### 4.2.1 Descent flight

The following numerical investigation concerns a descent flight with an inclination of  $-7$  degrees, at the velocity of 80 KIAS. Figure 13 and Figure 14 show the comparisons between the OASPL maps obtained by using aerodynamic data from fully coupled and uncoupled main and tail rotor aerodynamics. These maps are related to the OASPLs based on the 0-296 BPFs frequency range and, thus, include the high-frequency signal components. Most of the (slight) differences are located in small regions of the equatorial plane, as highlighted in Figure 15 that depicts the map of difference between the OASPLs of the two cases. Large regions of the acoustic map present differences lower than one dBA, thus revealing a negligible contribution of the interactional aerodynamics to the whole noise signature. This is an expected result because in this flight condition the acoustic emissions are strongly dominated by the Blade-Vortex-Interaction (BVI) noise. The tail rotor high-frequency contribution seems to provide, at least for this flight condition, a negligible contribution to the OASPL. This is demonstrated in Figure 16 that presents the OASPL map related to the 0-40 BPFs frequency range. Differences with the noise from the 0-296 BPFs frequency range are negligible (see Figure 13).

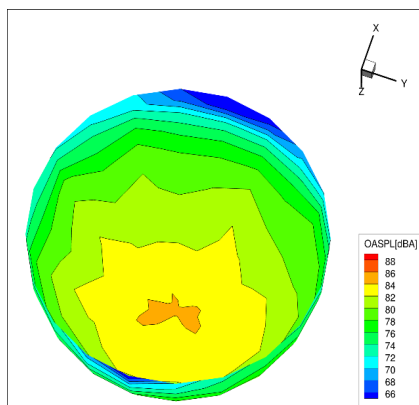


Figure 13: 0-296 BPFs OASPL [dBA], fully coupled aerodynamics, descending flight.

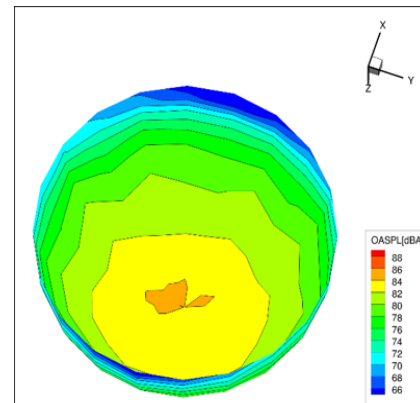


Figure 14: 0-296 BPFs OASPL [dBA], uncoupled main and tail rotor aerodynamics, descending flight.

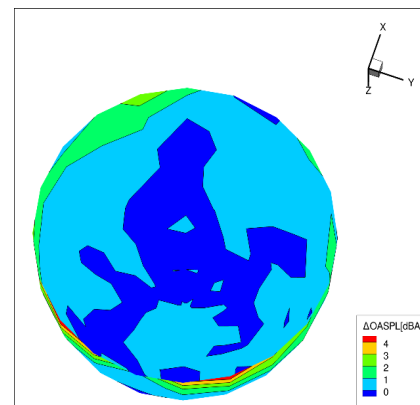


Figure 15: Difference of 0-296 BPFs OASPL [dBA] from fully coupled and uncoupled aerodynamics, descending flight.

#### 4.2.2 Forward flight

In this section, the results concerning a fly-over, forward flight condition at advancing velocity of 80 KIAS are considered. The acoustic impact is assessed through introduction of the same acoustic metrics applied in the previous section. Compared to the descent flight cases analyzed in Section 4.2.1, the present results for the noise signal magnitude are significantly different due to a clearly distinct main-tail rotors interactional aerodynamics, specially revealed in the tail rotor higher frequency contributions.

Specifically, as shown in Figure 17, Figure 18 and Figure 20, the values of the distributed OASPL are considerably lower than those observed for the descent flight, of about 16 dBA.

Furthermore, the main-tail rotor aerodynamic interactional effects seem to affect considerably the helicopter acoustic footprint, as proven by the comparison between the OASPL maps shown in Figure 17 and Figure 18. This is highlighted in Figure 19 that depicts the difference between the 0-296 BPFs OASPL obtained by using both interactional and non-interactional aerodynamic data. As opposed to Figure 15, wider portions of the maps show the differences in the range of 3-6 dBA. In addition, the higher frequency contribution from the tail rotor considerably alters the whole helicopter noise signature, which is demonstrated by the comparison between the magnitude and directivity patterns in Figure 17 for the 0-296 BPFs OASPLs and in Figure 20 for the 0-40 BPFs OASPL.

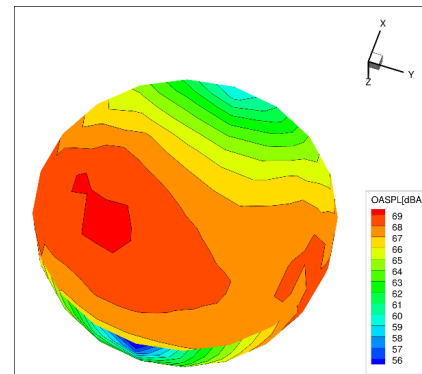


Figure 18: 0-296 BPFs OASPL [dBA], uncoupled main and tail rotor aerodynamics, forward flight.

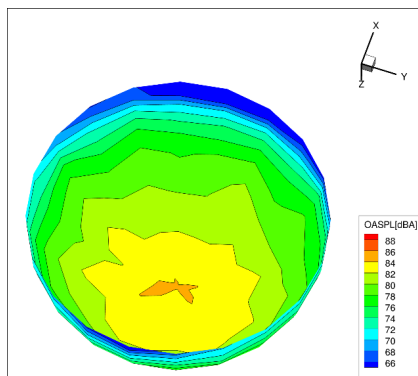


Figure 16: 0-40 BPFs OASPL [dBA], fully coupled aerodynamics, descending flight.

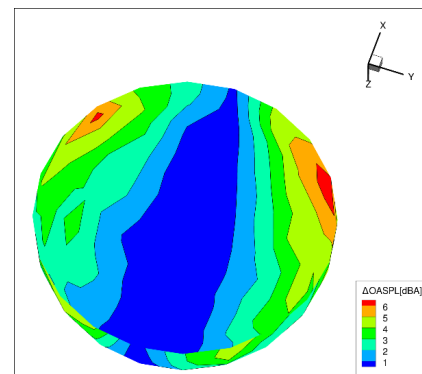


Figure 19: 0-286 BPFs OASPL [dBA], difference between fully coupled and uncoupled aerodynamics, forward flight.

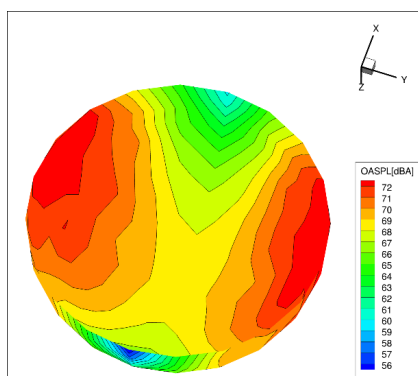


Figure 17: 0-296 BPFs OASPL [dBA] 0-296 BPFs, fully coupled aerodynamics, forward flight.

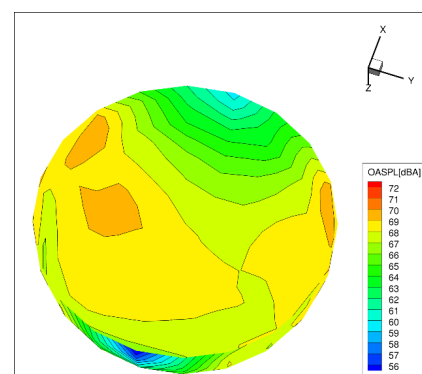


Figure 20: 0-40 BPFs OASPL [dBA], fully coupled aerodynamics, forward flight.

## 5. CONCLUSIONS

In this paper the detailed description of the structure of a new multi-disciplinary toolchain named CORAL (Comprehensive Rotorcraft Analyses Lab) for the analysis of VTOL vehicles in general configurations is presented. CORAL entirely modular structure allows for both continuous updates of its existent modules with the advance of the state of the art and the addition of new modules, further extending its present capabilities. Currently, CORAL allows for a fully integrated numerical nonlinear simulation of the aeromechanics and aeroacoustics of single and multiple rotors systems using cutting-edge structural, aerodynamics and aeroacoustics techniques. Moreover, CORAL is formulated to produce efficient linearized reduced-order models for cost-effective analyses of the more demanding numerical problems. Its structural module incorporates the multi-body dynamics method, permitting both the detailed representation of the rotors control chains and the modelling of composite blades undergoing arbitrarily large deformations using the geometrically exact beam theory. Its aerodynamic module includes different options that allow for a compromise between computational accuracy and fast solutions: a lower-fidelity actuator disk and blade element momentum model that is able to simulate rotors alone, a medium-fidelity free-vortex wake model, based on the potential Vortex-Particles Method with corrections for viscous effects due to drag, flow separation and compressibility effects, that offers the panel modelling of the fuselage and, ultimately, a high-fidelity hybrid methodology that combines for maximum effectiveness the conventional grid based CFD in the airframe near field with the grid-less particle method in the far field. The aeroacoustic module is based on the compact-source version of the Farassat 1A boundary integral formulation and it is currently able to model the complex interaction between the main and tail rotors of a conventional helicopter for the external noise radiation in different flight conditions.

In the present work, the preliminary result for a CORAL aeroelastic simulation case, the blade flatwise bending moment variation during one cycle in a forward-flight condition, is compared against the corresponding experimental result

obtained with the Kopter SH-09 helicopter, indicating a fairly good agreement. Also, noise footprint numerical simulations are presented for descending and forward-flight cases, demonstrating the capability of the CORAL aeroacoustic module to predict the effects of the main-tail rotors complex interactional aerodynamics on the overall helicopter noise signature.

## REFERENCES

- [1.] Gori R., Serafini J., Molica Colella M., Gennaretti M., "Assessment of a State-Space Aeroelastic Rotor Model for Rotorcraft Flight Dynamics," *CEAS Aeronautical Journal* 2016; **7**: 405-418. doi: 10.1007/s13272-016-0196-1.
- [2.] Gennaretti M., Muro D., "Multiblade Reduced-Order Aerodynamics for State-Space Aeroelastic Modeling of Rotors," *J. of Aircraft*, 2012; **49**: 495-502. doi: 10.2514/1.C031422.
- [3.] Riziotis V.A., Papadakis G., Manolas D.I., Voutsinas S.G., "A novel hybrid method for helicopter cost-effective aeroelastic simulations," 43<sup>rd</sup> European Rotorcraft Forum, Milan, Italy, Sept. 2017.
- [4.] Papadakis G., Voutsinas S.G., "A strongly coupled Eulerian Lagrangian method verified in 2D external compressible flows," *Computers & Fluids*, 2019; **195**:104325.
- [5.] Spyropoulos, N., Prospathopoulos, J., Manolas, D., Papadakis, G., Riziotis, V.A., "Development of a fluid structure interaction tool based on an actuator line model," Science of Making Torque from Wind Conference, 2020.
- [6.] Voutsinas S.G., *A GENeralized Unsteady Vortex Particle method for solving the unsteady flow around multi-component configurations*. Nat. Tech. Univ. Athens (NTUA), Internal Report, Athens, Greece, 1990.
- [7.] Petot, D., "Differential Equation Modelling of Dynamic Stall," *Recherché Aerospaciale*, 1989, **5**: 59-72.
- [8.] Roe P.L., "Characteristic-based schemes for the Euler equations," *Annual review of fluid mechanics*, 1986; **18**(1): 337-65.
- [9.] Venkatakrisnan V., "On the accuracy of limiters and convergence to steady state solutions," 31st Aerospace Sciences Meeting, Jan 1, 1993, (p. 880).

- [10.] Spalart P, Allmaras S., "A one-equation turbulence model for aerodynamic flows," 30th aerospace sciences meeting and exhibit, Jan 6, 1992 (p. 439).
- [11.] Menter F.R., "Two-equation eddy-viscosity turbulence models for engineering applications," *AIAA J.*, 1994; **32**(8): 1598-605.
- [12.] Vatsa V, Carpenter M, Lockard D., "Re-evaluation of an optimized second order backward difference (BDF2OPT) scheme for unsteady flow applications," 48th AIAA Aerospace Sciences Meeting Including the New Horizons Forum and Aerospace Exposition, 2010 (p. 122).
- [13.] Vatsa V, Turkel E., "Assessment of local preconditioners for steady state and time dependent flows," 34th AIAA Fluid Dynamics Conference and Exhibit, 2004 (p. 2134).
- [14.] Boisvert, R.F., "A fourth-order accurate fast direct method for the Helmholtz equation," *Elliptic Problem Solvers II*, 1984, 35-44.
- [15.] Colela G.T. Balls, Colella P., "A Finite Difference Domain Decomposition Method Using Local Corrections for the Solution of Poisson Equation," *J. Computational Physics*, 2002, **180**: 25.
- [16.] Hodges D.H., *Nonlinear Composite Beam Theory*, Progress in Aeronautics and Astronautics, Volume 213, AIAA, 2006.
- [17.] Yu W., *VABS Manual for Users*. Dept. Mech. & Aerospace Eng., Utah State Univ., Logan, Utah, 2011: 1–22.
- [18.] Etkin B., Reid L.D., *Dynamics of Flight: stability and control*. ISBN 0-471-03418-5. Canada: John Wiley & Sons, Inc., 1996. ISBN 978-88-203-2551-0.
- [19.] Arra M., *L'elicottero*, Hoepli, 2012, Milano, Italy. ISBN 978-88-203-2551-0.
- [20.] Leishman J.G., *Principles of Helicopter Aerodynamics*. Cambridge University Press, 2002. ISBN 0-521-66060-2.
- [21.] Gennaretti M., Bernardini G., "Aero-acousto-elastic modeling for response analysis of helicopter rotors," in *Variational Analysis and Aerospace Engineering Mathematical Challenges for Aerospace Design*. Springer US, 01 2012, pp. 27–50.
- [22.] Brentner, K.S., Jones, H.E., "Noise Prediction for Maneuvering Rotorcraft," 6th AIAA/CEAS Aeroacoustics Conference, AIAA, Paper 2000-2031, Lahaina, Hawaii, 2000.
- [23.] Lopes, L.V., "Compact Assumption Applied to Monopole Term of Farassat's Formulations," *J. of Aircraft*, 2017, **54**: 1649-1663.  
<https://doi.org/10.2514/1.C034048>.
- [24.] Bernardini, G., Gennaretti, M., Testa, C., "Spectral-Boundary-Integral Compact-Source Formulation for Aero-Hydroacoustics of Rotors," *AIAA J.*, 2016, **54**:3349-3360.  
<http://arc.aiaa.org/doi/abs/10.2514/1.J054923>.
- [25.] Ffowcs Williams, J.E., Hawkings, D.L., "Sound Generated by Turbulence and Surfaces in Arbitrary Motion," *Philosophical Transactions of the Royal Society, Series A: Mathematical and Physical Sciences*, 1969, **264**: 321-342.  
<https://doi.org/10.1098/rsta.1969.0031>.
- [26.] Brès, G.A., Brentner, K.S., Perez, G., Jones, H.E., "Maneuvering Rotorcraft Noise Prediction," *J. of Sound and Vibration*, 2004, **275**: 719-738.  
<https://doi.org/10.1016/j.jsv.2003.07.005>.
- [27.] Farassat, F., *Derivation of Formulations 1 and 1A of Farassat*. NASA TM 214853, 2007.
- [28.] Gennaretti M., Serafini J., Molica Colella M., Bernardini G., "Simulation of helicopter noise in maneuvering flight," 40th European Rotorcraft Forum, 2014, Southampton, UK.
- [29.] Gennaretti, M., Serafini, J., Bernardini, G., Castorrini, A., De Matteis, G., Avanzini, G., "Numerical Characterization of Helicopter Noise Hemispheres," *Aerospace Science and Technology*, 2016, **52**: 18-28.  
doi: 10.1016/j.ast.2016.02.013.
- [30.] Trainelli, L., Gennaretti, M., Bernardini, G., Rolando, A., Riboldi, C.E.D., Radaelli, M., Riviello, L., Scandroglio, A., "Innovative Helicopter In-Flight Noise Monitoring Systems Enabled by Rotor-State Measurements," *Noise Mapping*, 2016, **3**: 190-215.
- [31.] Gennaretti, M., Bernardini, G., Serafini, J., Anobile, A., Hartjes, S., "Helicopter Noise Footprint Prediction in Unsteady Maneuvers," *Int. J. of Aeroacoustics*, 2017, **16**: 165-180.  
doi: 10.1177/1475472X17709927.